Geochemistry Geophysics Geosystems G3

Article
Volume 14, Number 11
6 November 2013
doi: 10.1002/ggge.20281
ISSN: 1525-2027

Published by AGU and the Geochemical Society

Homogeneous bubble nucleation in rhyolitic melt: Experiments and nonclassical theory

H. M. Gonnermann
Department of Earth Science, Rice University, 6100 Main St., MS 126, Houston, Texas, 77005, USA (helge@rice.edu)

J. E. Gardner
Department of Geological Sciences, Jackson School of Geosciences, University of Texas at Austin, Austin, Texas, USA

[1] The transfer of volatiles from the Earth's interior to the atmosphere occurs through degassing of magma, the dynamics of which assert a significant control on volcanic eruptions. The first and most critical step in degassing is the nucleation of gas bubbles, which requires that a sufficient number of volatile molecules cluster together to overcome the free energy associated with the formation of a new interface between nucleus and surrounding melt. This free energy is a function of surface tension, typically assumed to equate to the macroscopically measurable value. Surface tension estimates inferred from bubble nucleation experiments in silicate melts are, however, lower than direct macroscopic measurements, making it difficult to accurately predict magma ascent and decompression rates from measured bubble number densities in pyroclasts. We provide a potential resolution to this problem through an integrated study of bubble nucleation experiments and modeling thereof, based on nonclassical nucleation theory. We find that surface tension between critical bubble nuclei and the surrounding melt depends on the degree of supersaturation and is lower than the macroscopically measured value. This is consistent with the view that far from equilibrium the interface between a nucleus and surrounding metastable bulk phase is diffuse instead of sharp. As a consequence, the increase in nucleation rate with supersaturation is significantly larger at high supersaturations than predicted by classical nucleation theory.

Components: 14,597 words, 12 figures, 1 table.

Keywords: nucleation theory; nonclassical nucleation theory; bubble nucleation; volcanic eruptions; magma degassing; explosive volcanism.

Index Terms: 8428 Explosive volcanism: Volcanology; 8445 Experimental volcanism: Volcanology; 8411 Thermodynamics: Volcanology; 8430 Volcanic gases: Volcanology; 8410 Geochemical modeling: Volcanology; 4302 Geological: Natural Hazards; 0766 Thermodynamics: Cryosphere; 1009 Geochemical modeling: Geochemistry; 1011 Thermodynamics: Geochemistry; 3610 Geochemical modeling: Mineralogy and Petrology; 3611 Thermodynamics: Mineralogy and Petrology.

Received 30 May 2013; **Revised** 24 September 2013; **Accepted** 1 October 2013; **Published** 6 November 2013.

Gonnermann, H. M., and J. E. Gardner (2013), Homogeneous bubble nucleation in rhyolitic melt: Experiments and nonclassical theory, *Geochem. Geophys. Geosyst.*, *14*, 4758–4773, doi:10.1002/ggge.20281.

1. Introduction

[2] Volcanism is the principal mechanism by which volatiles are transferred from the Earth's interior to its surface. The underlying process is magma degassing, a consequence of pressure-dependent solubilities of volatiles, such as H_2O and CO_2, in silicate melts. As magma rises toward the surface, and pressure decreases, the melt becomes supersaturated in volatiles. As a result, volatile-bearing bubbles nucleate and grow [*Toramaru*, 1989, 1995; *Gonnermann and Manga*, 2007], with the rates of bubble nucleation and growth largely determining the style by which the magma erupts [*Gonnermann and Manga*, 2007; *Houghton and Gonnermann*, 2008].

[3] As bubbles nucleate, the distance between individual bubbles, and hence the characteristic diffusion time of volatiles, decrease. Consequently, continuous bubble nucleation during magma ascent will eventually cause the diffusion of volatiles to be sufficiently fast to decrease supersaturation, despite further magma decompression. Magma decompression and bubble nucleation are thus competing processes that cause and inhibit supersaturation, respectively [*Toramaru*, 1989, 1995, 2006]. It is therefore possible to constrain magma ascent and decompression rates from the number of bubbles that nucleated in a given volume of melt upon eruptive magma ascent. To this end, a substantial body of research has been aimed at characterizing the size and abundance of bubbles (vesicles) in pyroclasts [e.g., *Sparks and Brazier*, 1982; *Toramaru*, 1989, 1990; *Mangan et al*., 1993; *Klug and Cashman*, 1994; *Gardner et al*., 1996; *Klug and Cashman*, 1996; *Mangan and Cashman*, 1996; *Blower et al*., 2001; *Polacci et al*., 2001; *Blower et al*., 2002; *Klug et al*., 2002; *Polacci et al*., 2003; *Gaonac'h et al*., 1996a, 1996b, 2005; *Polacci*, 2005; *Polacci et al*., 2006, 2009; *Gurioli et al*., 2005; *Adams et al*., 2006; *Lautze and Houghton*, 2007; *Piochi et al*., 2008; *Giachetti et al*., 2010; *Houghton et al*., 2010; *Alfano et al*., 2012].

[4] Bubble nucleation in magmas can be homogeneous, heterogeneous, or a combination of both [e.g., *Hurwitz and Navon*, 1994; *Mourtada-Bonnefoi and Laporte*, 1999; *Mangan and Sisson*, 2000; *Mourtada-Bonnefoi and Laporte*, 2002; *Gardner and Denis*, 2004; *Mourtada-Bonnefoi and Laporte*, 2004; *Mangan and Sisson*, 2005; *Gardner*, 2007; *Cluzel et al*., 2008; *Larsen*, 2008; *Hamada et al*., 2010; *Gardner and Ketcham*, 2011; *Gonde et al*., 2011]. In the case of heterogeneous nucleation, the abundant presence of impurities, such as crystals, provide nucleation substrates of lower interfacial energy. In some cases, however, the number density of bubbles in pyroclasts far exceeds the abundance of crystals which could act as nucleation substrates, suggesting that bubbles may have nucleated within the bulk metastable melt phase through homogeneous nucleation [e.g., *Debenedetti*, 1996]. Because the moments of the bubble size distribution, which are used to infer eruption dynamics, are a function of the nucleation rate [e.g., *Toramaru*, 1995], the ability to predict bubble nucleation rates is of essence to the study of volcanic eruptions. In this study, we solely focus on homogeneous bubble nucleation, because it constitutes the most fundamental bubble nucleation process and, thus, the basis for understanding bubble nucleation in magmas.

[5] Bubble nucleation is a consequence of random fluctuations in the spatial distribution of molecules of dissolved volatiles within the melt, resulting in the spontaneous formation of small molecular clusters. The rate of cluster formation increases with the supersaturation of volatiles that are dissolved within the melt phase. Supersaturation, in turn, is a consequence of magma decompression at faster rates than the rate at which volatiles can diffuse through the melt into bubbles, if they exist [e.g., *Toramaru*, 1989, 1995; *Navon et al*., 1998; *Navon and Lyakhovsky*, 1998; *Lensky et al*., 2004; *Toramaru*, 2006; *Gonnermann and Manga*, 2007]. For a given supersaturation, the free work associated with cluster formation increases with cluster size and reaches a maximum at a critical size, after which it decreases. This critical cluster size strongly depends on the change in energy associated with the formation of the vapor-melt interface. In other words, the critical cluster size depends on surface tension, with clusters larger than the critical size growing into bubbles, whereas smaller ones will not. Because the critical cluster size decreases with decreasing surface tension, the probability of cluster formation, that is the bubble nucleation rate, increases as surface tension decreases. Thus, the surface tension between the nucleating volatiles and the surrounding melt phase is of critical importance to bubble nucleation, magma degassing, and the dynamics of volcanic eruptions.

[6] The conventional theoretical framework within which the nucleation rate of bubbles is predicted is classical nucleation theory (CNT). It is based on the approximations that there exists an equilibrium distribution of nuclei and that these nuclei have the properties of the bulk phase. These approximations allow nucleation to be treated within a

thermodynamic framework, as opposed to a kinetic one [*Debenedetti*, 1996]. It is thus assumed that the surface tension between bubble nuclei and surrounding melt is the same as the surface tension that can be measured macroscopically. Close to equilibrium, the work of formation of a critical nucleus is in reasonable agreement with predictions from CNT, in part because the surface tension of the newly formed interface approaches that of a flat interface [*Kelton and Greer*, 2010]. With increasing departure from equilibrium, however, the interface between the new and original phases departs from capillarity (a sharp interface) and becomes diffuse. In the spinodal limit, far from equilibrium, surface tension and the work of formation of the new phase vanish. Consequently, the approximation of CNT that macroscopic properties of the bulk phase, and in particular surface tension, can be used to predict nucleation rates is strictly valid only close to equilibrium [*Kelton and Greer*, 2010]. With increasing departure from equilibrium this approximation no longer holds and surface tension is no longer constant. Instead, it may depend on the degree of departure from equilibrium, that is on the degree of supersaturation.

[7] One approach to studying bubble nucleation in magmas is the controlled decompression of silicate melt, which was equilibrated at some higher pressure with a volatile phase, usually H_2O [e.g., *Hurwitz and Navon*, 1994; *Mourtada-Bonnefoi and Laporte*, 1999, 2002, 2004; *Mangan and Sisson*, 2000, 2005; *Gardner and Denis*, 2004; *Gardner*, 2007; *Larsen*, 2008; *Hamada et al*., 2010; *Gonde et al*., 2011; *Nowak et al*., 2011; *Gardner and Ketcham*, 2011]. The resultant number of bubbles that nucleate within a volume of melt is then measured and divided by the duration of the experiment, typically of the order of 10–100 s, to obtain an average nucleation rate. Using CNT, together with the known supersaturation and other parameters, it is then possible to estimate the value of surface tension. As already pointed out, for example, by *Hamada et al.* [2010], typical values of surface tension thus obtained are significantly lower than those determined by direct measurements [*Bagdassarov et al*., 2000]. At the same time they are relatively high for producing the high bubble number densities observed in pyroclasts at magma decompression rates typically obtained from fluid dynamical modeling of magma ascent [*Toramaru*, 2006].

[8] To address this problem, we performed and modeled a suite of bubble nucleation experiments. During the experiments all parameters were known or controlled, except surface tension of the nucleating bubble. We focused on a single rhyolitic melt, in order to eliminate compositional dependencies, and on experiments within a narrow range of temperatures (±25°C), in order to limit the effect of temperature [*Walker and Mullins*, 1981; *Bagdassarov et al*., 2000; *Gardner and Ketcham*, 2011]. The only parameters that varied significantly were dissolved H_2O content and decompression rate. From the modeling of our experiments, we find that surface tension of the nucleating bubble is strongly dependent on the degree of supersaturation and is of lower value than the macroscopically measurable surface tension. These results are consistent with the contemporary framework of nonclassical nucleation theory.

[9] After a description of the experiments (section 2) we will, therefore, provide a discussion of nonclassical nucleation theory (section 3), as well as of our modeling approach for nonclassical bubble nucleation during the aforementioned experiments (section 4). This will be followed by a presentation of the results obtained from the modeling (section 5) and conclusions (section 6).

2. Bubble Nucleation Experiments

2.1. Samples and Experimental Techniques

[10] All experiments used cylinders drilled from a high-silica rhyolitic obsidian that consists of clear rhyolitic glass and less than 1 vol.% microlites of Fe-Ti oxides (Table 1). The composition of the glasses was determined by electron microprobe and, normalized to 100%, was in weight percent: 76.53% SiO_2, 0.06% TiO_2, 13.01% Al_2O_3, 0.79% FeO, 0.08% MnO, 0.02% MgO, 0.74% CaO, 3.87% Na_2O, and 4.91% K_2O, with Fe reported as FeO. Most cores were 2.2 mm in diameter and 1.1–1.3 cm long. All sharp edges were ground with emery paper to avoid piercing the metal tubing in which the cores were held during experiments. The cylinders were washed after being ground.

[11] Each experiment consisted of two steps: a sample was first hydrated with a given amount of water, and then decompressed to a lower pressure. For both hydration and decompression the pressure vessel was pressurized with water. For each hydration, a cylinder and distilled water were

Table 1. Experimental Conditions and Results[a]

Run	Starting Material	$p_{iniital}$ (MPa)	p_{final} (MPa)	T (°C)	Time	[H_2O] (wt.%)	N_m (m^{-3})
Hydration experiments							
G-1079	Rhyolite	120	120	900	144	4.27 ± 0.08	–
G-1088	Rhyolite	120	120	900	144	4.22 ± 0.01	–
G-1095	Rhyolite	140	140	900	120	4.71 ± 0.02	–
G-1096	Rhyolite	140	140	900	120	4.77 ± 0.04	–
G-591*	Rhyolite	160	160	875	120	5.01 ± 0.18	–
G-594*	Rhyolite	160	160	875	120	5.17 ± 0.50	–
G-595*	Rhyolite	160	160	875	120	4.93 ± 0.13	–
G-610*	Rhyolite	160	160	875	120	5.00 ± 0.03	–
G-630*	Rhyolite	160	160	875	120	4.81 ± 0.14	–
G-644*	Rhyolite	160	160	875	120	4.90 ± 0.08	–
G-695*	Rhyolite	160	160	875	120	4.95 ± 0.05	–
G-876*	Rhyolite	160	160	875	120	5.08 ± 0.01	–
G-882*	Rhyolite	160	160	875	120	5.03 ± 0.01	–
G-883*	Rhyolite	160	160	875	120	4.93 ± 0.05	–
G-885*	Rhyolite	160	160	875	120	5.00 ± 0.01	–
G-931*	Rhyolite	160	160	875	120	5.03 ± 0.02	–
G-1121	Rhyolite	200	200	875	120	5.62 ± 0.06	–
G-1140	Rhyolite	200	200	875	120	5.66 ± 0.02	–
G-1147	Rhyolite	200	200	875	120	5.52 ± 0.02	–
G-1231	Rhyolite	210	210	850	120	5.58 ± 0.02	–
Decompression experiments							
G-906*	G-883	161 (146)	51.5	825	10/50	–	0
G-938*	G-931	161 (151)	37	825	10/50	–	7.35×10^{8}
G-890*	G-882	161 (151)	22	825	10/50	–	2.26×10^{8}
G-907*	G-885	161 (150)	15	825	16/44	–	4.95×10^{8}
G-889*	G-876	161 (154)	8.5	825	10/50	–	7.84×10^{10}
G-1233	G-1231	211	24.5	850	14/46	–	$4.4 \times 10^{13(\#)}$
G-1234	G-1231	211	23.5	850	10/20	–	$6.8 \times 10^{13\ (\#)}$
G-1089	G-1079	121	18	875	8/52	4.23±0.03	0
G-1149	G-1088	121	10	875	22/38	–	0
G-1110	G-1095	141	46.5	875	20/40	–	0
G-1113	G-1096	141	43.5	875	5/55	–	0
G-1112	G-1096	141	34	875	12/48	–	3.12×10^{8}
G-1111	G-1095	141	23	875	16/44	–	1.40×10^{9}
G-660*	G-630	161	80	875	5/55	–	0
G-593*	G-591	161	65	875	3/57	–	0
G-724*	G-695	161	52.5	875	10/50	–	2.5×10^{8}
G-658*	G-610	161	47	875	8/52	–	4.76×10^{8}
G-604*	G-594	161	33	875	20/40	–	2.91×10^{9}
G-665*	G-644	161	22.5	875	9/51	–	2.14×10^{9}
G-608*	G-595	161	13.5	875	11/109	–	3.21×10^{10}
G-1129	G-1121	201	100	875	17/43	–	0
G-1159	G-1147	201	85.5	875	10/48	–	0
G-1148	G-1140	201	74.5	875	35/25	–	5.93×10^{9}

[a] $p_{initial}$ and p_{final} are the initial and final pressures of the experiment; Times are either hours at hydration pressure, or number of seconds it took to lower pressure to p_{final} (±1 s) and number of seconds the sample remained at p_{final}; [H_2O] is total water content (±1σ); N_m is the number density of bubbles nucleated, determined by counting numbers of bubbles in given volumes of the sample, except (#) for which N_m was determined from measured bubbles sizes and porosity (see text for discussion). Experiments indicated by * were also reported in *Gardner and Ketcham* [2011].

added to a 4 mm O.D. Au capsule, which had been welded at one end. Enough water, usually ca. 10% by weight of the cylinder, was added to ensure that a fluid existed throughout the hydration. Then, the capsule was crimped, weighed, and welded shut. The sealed capsule was then heated on a hotplate for 10–15 min and weighed again to check for leaks. All hydrations were carried out in externally heated, cold-seal pressure vessels, made of a Nickel-based alloy, and were run at 850°C, 875°C, or 900°C and various pressures for 5 days (Table 1). The samples were absolutely crystal free after this hydration step. *Gardner et al*. [1999] showed that samples hydrated at superliquidus conditions for 5 days result in homogeneous nucleation, whereas samples hydrated for 3 or less days resulted in heterogeneous nucleation, despite the apparent absence of any crystals suitable as bubble nucleation sites. We thus conclude that our sample preparation resulted in experiments where bubbles nucleated homogeneously within the bulk of the melt.

[12] Pressure was measured to ±0.1 MPa, and the K-type thermocouples used have been found to be

precise to ±5°C. The use of a Ni filler rod in the pressure vessel ensured that the sample hydrated at an oxygen fugacity similar to the Ni-NiO oxygen buffer [*Gardner et al*., 1995]. Samples were quenched by removing the pressure vessel from the furnace and, after blowing on the vessel with compressed air until it stopped glowing red, immersing it into a bucket of water. The hydrated glass cylinder was then extracted from the capsule and split; one piece was used to measure dissolved water contents by Fourier transform infrared spectroscopy (see below), the other in a decompression experiment.

[13] Decompression experiments consisted of hydrated cylinders inside Au capsules welded shut. Each capsule was placed into a cup on the end of an Inconel rod and inserted into an externally heated, cold-seal pressure vessel fitted with a rapid-quench extension. The sample was held in the water-cooled region of the vessel while the pressure vessel heated to 825–875°C. Because the pressurizing medium was water, the adiabatic temperature drop during depressurization is smaller than in experiments that are pressurized by compressed gas [e.g., *Hamada et al*., 2010], with the difference in temperature between initial hydration and decompression corresponding in all cases to a solubility difference of <0.1 wt.% [e.g., *Liu et al*., 2005]. We thus expect a negligible effect on the experimental results.

[14] Once the pressure vessel thermally equilibrated, the sample rod was raised with a magnet to insert the sample into the hot zone of the pressure vessel. The pressure was quickly adjusted using a hand-operated intensifier to 1 MPa above the hydration pressure to discourage water loss from the melt during heating. After the sample heated for 5 min, pressure was released manually within 3–35 s to a lower final pressure (Table 1). After samples reached their final pressures, most of them were held at that pressure until a total of 60 s had elapsed, including the time during which pressure was decreased. Samples were then quenched rapidly by lowering the magnet, which brought the sample back into the water-cooled jacket. One experiment (G-1234) was quenched after only a total of 30 s had elapsed, whereas G-608 was quenched only after 120 s had elapsed.

[15] After being quenched, each capsule was removed from its pressure vessel, checked that it had remained sealed, and then the sample was removed and sectioned for analysis. The number density of bubbles, $N_{m,\mathrm{obs}}$, that nucleated was determined by selecting 4–5 areas (40 μm × 40 μm) of a sample and counting all bubbles that appear as the field of view is moved through the sample using the focusing knob of the microscope. If bubbles had a shape indicative of two bubbles quenched in the act of merging, then we counted the two separately. The depth viewed was usually between 800 μm and 2000 μm, and measured using a Heidenhain focus drive linear encoder. The average error is ± 0.6 μm, determined by repeatedly focusing through a sample. In two cases, bubbles were too numerous to count individually. In those cases, number densities were calculated from porosity and bubble sizes in the experiments, modified from *Gardner et al*. [1999]

$$N_m = \frac{\phi N_{\mathrm{tot}}}{(1-\phi)\sum (n_i V_i)}, \qquad (1)$$

in which n_i and V_i are the number and volume of bubbles of diameter i, respectively, N_{tot} is the total number of bubbles measured, and ϕ is the volume fraction of bubbles.

[16] All hydration samples were analyzed for dissolved water contents by Fourier transform infrared (FTIR) spectroscopy, using a Thermo Electron Nicolet 6700 spectrometer and Continuum IR microscope. Three to six spectra were collected, with each spectrum consisting of 60 scans at a resolution of 4 cm^{-1}, and measured in transmittance mode in the near-IR region (7800–4000 cm^{-1}) with white light and a CaF_2 beamsplitter. Contents of molecular water (H_2O_m) and hydroxyl water (OH^-) were determined from absorbances at ≈ 5250 cm^{-1} and ≈ 4500 cm^{-1}, respectively, using the model of *Zhang et al*. [1997], and the thickness where each spectrum was collected measured with the method described above. Water contents reported are the averaged sums of H_2O_m and OH^- contents (Table 1). Water contents in one decompression sample were measured at various positions through the sample.

2.2. Experimental Results

[17] All hydrations produced crystal- and bubble-free glasses. Samples that were hydrated at 120–210 MPa, producing initial water contents that range from 4.2 to 5.7 wt.% (Table 1). At a given pressure, H_2O contents differ by only a few percent and agree well with those predicted by the solubility models of *Gardner et al*. [1999] and *Liu et al*. [2005], with an average difference of <2% between measured and model amounts. All

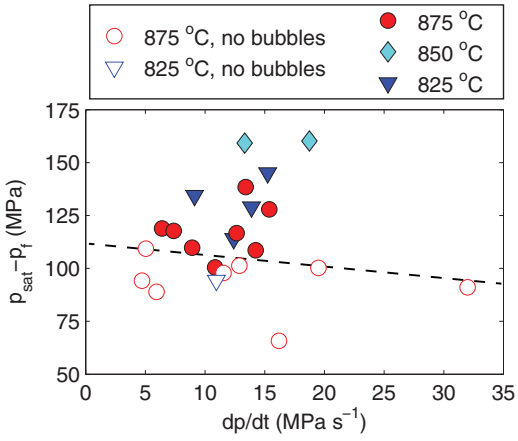

Figure 1. Difference of saturation pressure, p_{sat}, and final pressure, p_f, as a function of decompression rate, dp/dt. The threshold between homogeneous bubble nucleation (solid symbols) and no nucleation (open symbols) approximately correlates with $p_{sat}-p_f$, as indicated by the dashed line.

decompressed samples contained numerous small "fringe" bubbles at or very near the contact of the sample with the capsule wall, which result from heterogeneous nucleation along the contact [*Mangan and Sisson*, 2000]. We ignore those and measured only bubbles that nucleated in the interiors for our analysis. Because bubble nucleation depends on the degree of supersaturation, which is quantified as the difference between saturation pressure and actual pressure, we must calculate the saturation pressure, p_{sat}, of each sample. It is equal to the pressure at which the melt is saturated with the measured concentration of H_2O, according to the solubility model of *Liu et al*. [2005]. Similarly, we used the model of *Liu et al*. [2005] to estimate H_2O contents expected at final pressures, p_f. Water contents were measured in one decompressed sample that did not nucleate bubbles and found to match those of the hydrated sample used. We conclude that no water diffused out of the samples during the 60 s at low pressure.

[18] Final pressures, p_f, ranged from 8.5 MPa to 100 MPa (Table 1). Decompression rates ranged between approximately 4 MPa s^{-1} and 32 MPa s^{-1} (Figure 1) and are defined as the difference between initial and final pressures divided by the time required to reach final pressure after the onset of decompression. Within the range of examined decompression rates, there was no significant correlation between decompression rate and whether bubbles nucleated or not during a given experiment. Similarly, whether bubbles nucleated did not significantly depend on p_{sat}, but rather appears to first-order dependent on the difference between p_{sat} and p_f (Figures 1 and 2), with no bubbles nucleating at approximately $(p_{sat}-p_f) < 100$ MPa during a time interval of 60 s. The requirement of such large supersaturations to trigger bubble nucleation further argues that nucleation is homogeneous.

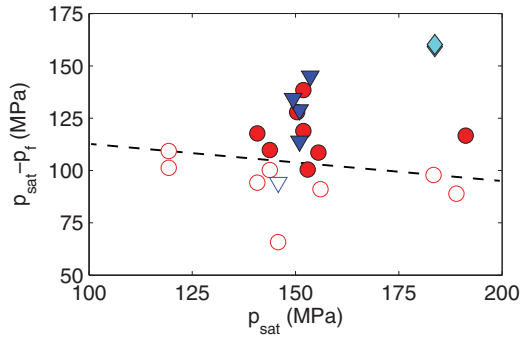

Figure 2. Difference of saturation pressure, p_{sat}, and final pressure, p_f, as a function of p_f. The threshold between homogeneous bubble nucleation (solid symbols) and no nucleation (open symbols) approximately correlates with $p_{sat}-p_f$, as indicated by the dashed line. Symbols are the same as in Figure 1.

[19] The range of initial water contents used for our experiments was within the range of pre-eruptive water contents of many natural rhyolites [e.g., *Wallace*, 2005, and references therein], which is considerably lower than those used in some previous decompression-nucleation experiments of rhyolitic melts [e.g., *Mourtada-Bonnefoi and Laporte*, 2004; *Hamada et al*., 2010]. In contrast to these previous experiments, the number density of homogeneously nucleated bubbles, N_m, spanned a wider range, from approximately 10^8 m^{-3} to 10^{14} m^{-3}, and to first order depends on the degree of supersaturation ($p_{sat}-p_f$), as shown in Figure 3. We speculate that such a dependence was not found in previous experiments [e.g.,

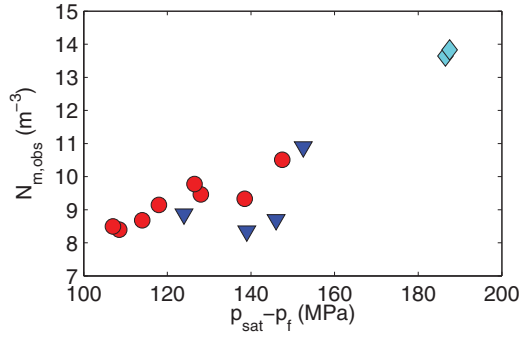

Figure 3. Bubble number density, N_m, as a function of supersaturation pressure, $p_{sat}-p_f$, indicating the N_m is to first-order dependent on $p_{sat}-p_f$. Symbols are the same as in Figure 1.

Mourtada-Bonnefoi and Laporte, 2004; *Hamada et al*., 2010] because of the higher and more narrow range of initial water contents used.

3. Nucleation Theory

3.1. Classical Theory of Stationary Nucleation

[20] The spontaneous formation of molecular clusters is associated with a decrease in free energy, resulting from cluster formation and an increase in free energy, caused by the creation of an interface between the nucleus and the metastable liquid phase. The sum of these changes in free energy has a maximum at a critical cluster size, above which the addition of new molecules to the cluster is energetically favorable.

[21] In classical nucleation theory, the spontaneous rate of cluster formation of critical size is based on an assumed steady state, obtained from the dimensionless Zeldovitch factor, Z, and the frequency, ω, of formation of nuclei, is larger than the critical size [e.g., *Hirth et al*., 1970; *Hurwitz and Navon*, 1994; *Debenedetti*, 1996; *Mourtada-Bonnefoi and Laporte*, 2002]. They are given by

$$Z = \frac{\Omega_L (p_b - p)^2}{8\pi\sigma^{3/2}\sqrt{k_B T}} \tag{2}$$

and

$$\omega = \frac{16\pi\sigma^2 n_0 D}{a_0 (p_b - p)^2}, \tag{3}$$

where Ω_L is the molecular volume of water, $k_B = 1.38 \times 10^{-23}\,\mathrm{J\,K^{-1}}$ is the Boltzmann constant and T is an absolute temperature. n_0 is the number of water molecules per unit volume, $a_0 \approx (n_0)^{-1/3}$ is the distance between molecule centers, and σ is the interfacial tension between bubble nucleus and melt phase, assumed to be a constant and equal to the value at equilibrium conditions, σ_∞.

[22] The supersaturation pressure ($p_b - p$) describes the degree of disequilibrium, where p_b is the internal pressure of the critical nucleus and p is the ambient pressure of the melt phase. In general, p_b will be smaller than the saturation pressure of the melt, p_{sat}, and can be calculated from [*Debenedetti*, 1996; *Cluzel et al*., 2008]

$$\Gamma(p_b, T)\, p_b = \Gamma(p_{sat}, T)\, p_{sat}\, e^{\Omega(p - p_{sat})/k_B T}, \tag{4}$$

where $\Gamma(p_b, T)$ and $\Gamma(p_{sat}, T)$ are the fugacity coefficients of the volatile phase at the specified pressure and temperature.

[23] Based on the above definitions, the stationary nucleation rate, based on the classical theory, can be written as [*Hirth et al*., 1970; *Hurwitz and Navon*, 1994; *Mourtada-Bonnefoi and Laporte*, 2002]

$$J_{cls} = A e^{-W_{cl}/k_B T}. \tag{5}$$

[24] Here, W_{cl} is the classical work of nucleus formation, first derived by *Gibbs* [1961]. The coefficient, A, is defined as

$$A = \frac{2\Omega n_0^2 D}{a_0}\sqrt{\frac{\sigma_\infty}{k_B T}}, \tag{6}$$

where in our case D is the diffusivity of H_2O in the metastable melt phase.

[25] W_{cl} depends on a single unknown quantity, the surface tension between bubble nucleus and melt phase, and is given by

$$W_{cl} = \frac{16\pi\sigma_\infty^3}{3(p_b - p)^2}. \tag{7}$$

[26] It is important to note that in this definition surface tension between bubble nucleus and melt phase is considered equivalent to the macroscopically measurable interfacial tension between the magmatic vapor phase and the melt phase, σ_∞, where the subscript ∞ denotes an interface of large radius of curvature, compared to a critical nucleus.

3.2. Nonstationary Nucleation

3.2.1. Nucleation Time Lag

[27] The finite time required for nucleation to reach steady state can be characterized by τ_l, the nucleation time lag [e.g., *Debenedetti*, 1996; *Kashchiev*, 2000; *Mourtada-Bonnefoi and Laporte*, 2002]. The value of τ_l can be calculated as

$$\tau_l = \frac{4}{\pi^3 \omega Z^2}. \tag{8}$$

[28] The nonstationary nucleation rate, J_{clt} (t), is given by [*Debenedetti*, 1996]

$$J_{\mathrm{clt}}(t) = J_{\mathrm{cls}}[1 - \exp(-t/\tau_l)], \tag{9}$$

where t is the time. An alternate formulation yielding similar results is given by *Kashchiev* [2000] as

$$J_{\mathrm{clt}}(t) = J_{\mathrm{cls}}\left[1 + 2\sum_{i=1}^{\infty}(-1)^i \exp\left(-i^2 t/\tau_l\right)\right]. \tag{10}$$

[29] For hydrated rhyolitic melt $\tau_l \sim 10^{-6}$ s implying that steady state is reached after $<10\ \tau_l \sim 10^{-5}$ s. Consequently, $J_{\mathrm{clt}} \approx J_{\mathrm{cls}}$ is a valid approximation and we shall use J_{cl} as the classical nucleation rate throughout the remainder of this discussion, in lieu of J_{clt} or J_{cls}.

3.2.2. Induction Time

[30] The induction time, τ_i, also referred to as induction period, is the time that elapses until an appreciable number of bubbles are experimentally observable [*Kashchiev*, 2000]. A practical estimate of τ_i is [*Kashchiev*, 2000]

$$\tau_i = b_{i,m}\tau_l + \frac{1}{JV}, \tag{11}$$

where $b_{i,m} \approx 1$, V is the volume of the system and J is the actual nucleation rate. For small values of τ_l, as is the case here,

$$\tau_i \approx \frac{1}{JV}. \tag{12}$$

[31] As discussed in section 2, a subset of experiments had induction times that were greater than the duration of the experiment and did not nucleate bubbles (Table 1).

3.3. Nonclassical Theory for Thermodynamically Consistent Work of Nucleus Formation

[32] The classical nucleation work, W_{cl}, is in principle valid for all possible values of thermodynamic parameters of the metastable phase, that is density fluctuations and nucleus size. The value of σ, however, is usually only measurable for macroscopic conditions, where its value is expected to be larger than the surface tension associated with a critical cluster [*Kashchiev*, 2003, 2004], for which the interface is thought to be diffuse instead of sharp. To overcome this limitation, *Kashchiev* [2003, 2004] derived a higher-order approximation of the nucleation work, W_{nc}, that permits the use of the macroscopic value of σ, but is, nevertheless, valid across the whole range of nucleus sizes.

[33] Kashchiev's formulation for the stationary nonclassical nucleation rate is

$$J_{\mathrm{nc}} = Ae^{-W_{\mathrm{nc}}/k_{\mathrm{B}}T}. \tag{13}$$

[34] It is based on the ratio of the nonclassical nucleation work to the classical value and is given by the approximation

$$\frac{W_{\mathrm{nc}}}{W_{\mathrm{cl}}} \approx 1 - \xi^2. \tag{14}$$

[35] Here, W_{nc} is defined as

$$W_{\mathrm{nc}} = \frac{16\pi\sigma_{\mathrm{nc}}^3}{3(p_{\mathrm{b}} - p)^2} \tag{15}$$

and ξ is defined as the normalized supersaturation pressure

$$\xi = \frac{p_{\mathrm{b}} - p}{\Delta p^*} = \frac{\Delta p_s}{\Delta p^*}. \tag{16}$$

[36] Δp^* is a reference pressure, conventionally taken as the difference between p_{b} and the pressure at the spinodal, assuming it exists. This formulation is thermodynamically consistent in the sense that the classical value of W_{nc} is recovered at $\xi \to 0$, whereas the nucleation energy vanishes at $\xi \to 1$. The corresponding value of σ_{nc} is given by

$$\sigma_{\mathrm{nc}} = \sigma_\infty\left(1 - \xi^2\right)^{1/3}. \tag{17}$$

4. Modeling Approach

[37] During each experiment, the hydrated melt was decompressed at an almost constant temperature, T, from the initial pressure, p_{initial} at time $t = 0$, to the final pressure, $p = p_{\mathrm{final}}$ at time $t = \tau_{\mathrm{dec}}$. During the time interval $0 \le t \le \tau_{\mathrm{dec}}$, the supersaturation pressure, Δp_s, steadily increased, unless the characteristic time scale of water diffusion into growing bubbles [e.g., *Lensky et al.*, 2004; *Gonnermann and Manga*, 2007] became shorter than the characteristic decompression time before $t = \tau_{\mathrm{dec}}$ was reached. After decompression, the sample was held at $p = p_{\mathrm{final}}$ for a duration of $\tau_{\mathrm{final}} - \tau_{\mathrm{dec}}$, at which time the sample was abruptly quenched. For all experiments $3 \le \tau_{\mathrm{dec}} \le 35$ s and τ_{final} was either 30, 60, or 120 s (Table 1).

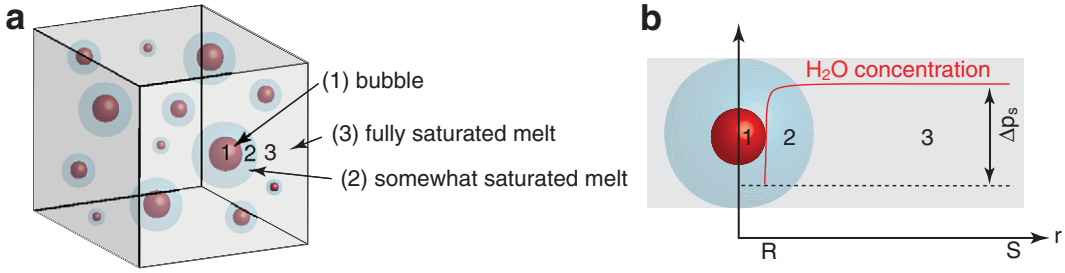

Figure 4. (a) Schematic representation of the modeled melt volume [*Kedrinskiy*, 2009]. (1) represents the bubble; (2) the diffusion envelope that is the part of the melt where volatile concentrations and correspondingly nucleation rates are low; and (3) is the nucleation region. During most of the modeling, the volume fraction of melt comprised by region (3) is close to a value of 1. (b) Schematic graph of volatile concentration in the melt as a function of radial distance, r, where R is the bubble radius and S is the radius of the surrounding melt shell. The difference between the saturation pressure at the actual volatile concentration (solid red curve) and the equilibrium concentration at the pressure inside a bubble nucleus is the supersaturation pressure.

[38] We model bubble nucleation over the entire time interval $0 \leq t \leq \tau_{\text{final}}$. In some experiments, and model simulations thereof, the nucleation work, W_{nc}, was too high and nucleation rates too low for any bubbles to nucleate within the sample over the duration of the experiment, that is $\tau_{\text{final}} < \tau_i$ and $N_m = 0$. For most experiments, however, nucleation rates were sufficiently high for bubbles to begin to nucleate after some time and to continue nucleating until the end of the experiment, or until volatile diffusion begins to deplete the melt of H_2O supersaturation and nucleation ceases.

[39] Once a bubble has nucleated, H_2O diffuses from the melt into the bubble. Hence, the concentration of H_2O in the melt will no longer be uniform throughout the melt volume (Figure 4). Consequently, both bubble nucleation and growth need to be modeled in order to estimate the degree of volatile supersaturation throughout the melt volume, which in turn affects the rate of bubble nucleation. We will first summarize the methodology for bubble growth modeling in section 4.1 and subsequently discuss the approach to modeling of bubble nucleation in section 4.2.

4.1. Modeling Bubble Growth

[40] We assume that the size of the critical bubble nucleus can be derived from the Laplace relation, which describes the mechanical equilibrium condition for a bubble

$$p_g - p = \frac{2\sigma_\infty}{R}, \tag{18}$$

where p_g is the pressure inside the bubble and R its radius. The critical bubble radius, R_c, that satisfies equation (18) is given by [e.g., *Proussevitch et al.*, 1993]

$$R_c = \frac{2\sigma_\infty}{\Delta p_s}. \tag{19}$$

[41] Typically, R_c is of the order of 1–10 nm and if $R < R_c$, the bubble will shrink and disappear. Because the value of σ_{nc} is not known a priori, we use σ_∞ instead of σ_{nc} in equation (19). The difference between the two values is at most a factor of two and, as already discussed in *Gonnermann and Houghton* [2012], small variations in surface tension do not sufficiently affect the diffusive bubble growth calculations.

[42] Bubble growth is a consequence of the volume expansion of the already exsolved H_2O vapor and the diffusion of H_2O from the melt into existing bubbles. The latter typically accounts for about 99.90–99.99% of the final bubble volume, with final bubble radii typically of the order of 10^{-5}–10^{-4} m. The mass flux of H_2O into each bubble is determined by the concentration gradient in the melt at the melt-vapor interface, that is at radius $r = R$. It is calculated as

$$q = D\left(\frac{\partial c}{\partial r}\right)_{r=R}. \tag{20}$$

[43] The diffusivity of H_2O within rhyolite melt, D, is based on the formulation of *Ni and Zhang* [2008]. The value of q is calculated from a diffusion model for bubble growth [e.g., *Amon and Denson*, 1984; *Arefmanesh and Advani*, 1991; *Proussevitch et al.*, 1993], wherein bubbles are assumed to be spatially distributed, such that each bubble can be approximated as a sphere

surrounded by a spherical melt shell of thickness $S-R$ (Figure 4). Because of the spherical symmetry inherent in this approximation, volatile diffusion simplifies to

$$\frac{\partial c}{\partial t} + v_r \frac{\partial c}{\partial r} = \frac{1}{r^2}\frac{\partial c}{\partial r}\left(Dr^2 \frac{\partial c}{\partial r}\right), \tag{21}$$

where $v_r = dR/dt$ is the radial velocity of melt at $r = R$. Equation (21) is solved using an implicit finite difference scheme, employing a Lagrangian frame of reference, a nonuniform grid [*Arefmanesh and Advani*, 1991; *Proussevitch et al*., 1993] and a Neumann boundary condition at $r = S$, given by

$$\left(\frac{\partial c}{\partial r}\right)_{r=S} = 0. \tag{22}$$

[44] Mass conservation of H_2O requires that

$$\frac{d}{dt}\left(\rho_g R^3\right) = 4R^2 \rho_m q, \tag{23}$$

where ρ_m is the melt density and the density of the exsolved gas phase, denoted as ρ_g, depends on p_g via an equation of state. Here, we use the modified Redlich-Kwong equation of state of *Kerrick and Jacobs* [1981].

[45] Bubble growth is resisted by viscous and capillary stresses, which are balanced by the pressure difference between the gas mixture inside the bubble and the surrounding melt

$$p_g(t) - p(t) = \frac{2\sigma_\infty}{R} + 4\eta_e \frac{1}{R}\frac{dR}{dt}. \tag{24}$$

[46] The effective viscosity, η_e, accounts for the radially variable, H_2O-dependent Newtonian viscosity of the melt [*Lensky et al*., 2001; *Hui and Zhang*, 2007].

[47] Bubble growth for a representative bubble, nucleated at time t_i, is calculated for the time interval $(t_i \le t \le t_{\text{final}})$. At each bubble-growth time step the coupled equations (21), (23), and (24) are solved iteratively until convergence of p_g, similar to the methodology described in *Proussevitch et al*. [1993]. This results in the required data arrays $c_{i,k}$ and $v_{i,k}$, which are subsequently used during the calculation of bubble nucleation, in order to estimate the degree of supersaturation throughout the modeled melt volume.

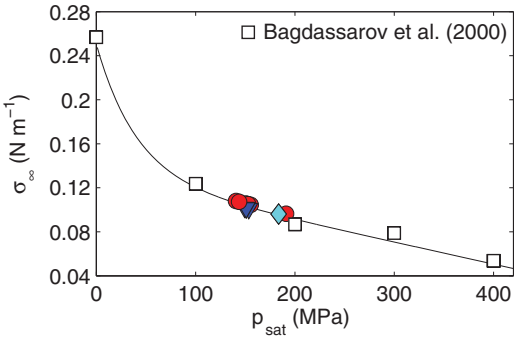

Figure 5. The value of σ_∞ used to calculate W_{cl} (equation (7)). The value of σ_∞ is based on a fit of measured surface tension values of haplogranitic melt at 1000°C, adjusted to the corresponding temperatures of 825°C, 850°C, and 875°C [*Bagdassarov et al*., 2000], using $d\sigma/dT = 7.5 \times 10^{-5}\text{Nm}^{-1}\,^{\circ}\text{C}^{-1}$ [*Bagdassarov et al*., 2000]. Solid squares are the measured values of *Bagdassarov et al*. [2000] adjusted to 850°C, all other symbols are the same as in Figure 1.

4.2. Modeling Bubble Nucleation

[48] We calculate the number of bubbles that nucleate during the time interval $t_i \le t \le t_i + \Delta t$ and within a given subvolume of melt, $v_{i,k}$, as

$$n_{i,k} = v_{i,k} J_{\text{nc}}(i,k)\Delta t. \tag{25}$$

[49] Here $t_i = i\Delta t$ and $J_{\text{nc}}(i,k)$ is calculated from equation (13) for the average concentration of H_2O at time $t_i + \Delta t/2$ and within the subvolume of melt denoted by the subscript $k = 1 \ldots m$. The value of $J_{\text{nc}}(i,k)$ depends on the pressure p at time $t_i + \Delta t/2$, as well as on the average H_2O concentration at that time and within the given subvolume of melt $v_{i,k}$. Here, the spatio-temporal distribution of H_2O concentration is, as already discussed in section 4.1, obtained from the diffusive bubble growth calculations. The total volume of bubbles at time $t_i + \Delta t/2$ within the entire melt volume is then calculated as

$$N_m(t_i) = \sum_{j=1}^{i}\left(\sum_{k=1}^{m} n_{j,k}\right). \tag{26}$$

[50] The value of $\sigma_{\text{nc}}(t_i)$ required for the calculation of J_{nc} is calculated from equation (17), which is based on contact angle measurements of σ_∞ for haplogranitic melt by *Bagdassarov et al*. [2000], albeit extrapolated to the temperature of our experiments using $d\sigma/dT = 7.5 \times 10^{-5}\text{Nm}^{-1}\,^{\circ}\text{C}^{-1}$ [*Bagdassarov et al*., 2000]. The resultant values of σ_∞ for both the contact angle measurements and our experiments are shown in Figure 5.

5. Results and Discussion

[51] We modeled homogeneous bubble nucleation in the experiments of section 2 by integrating equation (26), which requires the calculation of J_{nc} and, hence, σ_{nc}. The latter is estimated from equation (17), wherein the value Δp^* is not known a priori. For each experiment, we therefore repeated the entire analysis over a range of Δp^*, with the objective of finding a value for Δp^*, that minimizes the difference between observed and predicted bubble number densities. The match between observed and calculated values of N_m is quantified as a misfit, $0 \leq \chi \leq 1$, which is defined as

$$\chi = |N_{m,\mathrm{pred}}/N_{m,\mathrm{obs}} - 1| \text{for } N_{m,\mathrm{pred}} < N_{m,\mathrm{obs}}, \quad (27a)$$

$$\chi = |N_{m,\mathrm{obs}}/N_{m,\mathrm{pred}} - 1| \text{for } N_{m,\mathrm{pred}} \geq N_{m,\mathrm{obs}}. \quad (27b)$$

[52] For each experiment, the value of χ, as a function of Δp^*, is shown in Figure 6. For all cases a unique and well-defined minimum identifies the value of Δp^* at which $\chi \ll 0.01$ and $N_{m,\mathrm{pred}} \approx N_{m,\mathrm{obs}}$. For experiments where $N_{m,\mathrm{obs}}$ is small, relatively modest changes in Δp^* result in a large change in $N_{m,\mathrm{pred}}$, relative to $N_{m,\mathrm{obs}}$. Consequently, χ has a narrow minimum. In contrast, for larger values of $N_{m,\mathrm{obs}}$ there is a broader minimum in χ, because at a given change in Δp^* the change in $N_{m,\mathrm{pred}}$, relative to $N_{m,\mathrm{obs}}$, is smaller.

[53] Two contrasting examples of combined bubble nucleation and growth modeling are shown in Figure 7. In the case of G-1112, nucleation rates and resulting bubble number densities were too low for water diffusion into existing bubbles to significantly affect the supersaturation of most of the sample. Consequently, most of the sample remained fully saturated (e.g., Figure 4) and bubbles nucleated until the sample was quenched after 60 s. In contrast, for G-1233 nucleation rates and resulting bubble number densities were high. Water diffused into existing bubbles from the entire melt volume within a short time after the onset of nucleation and, consequently, there was only a short burst of nucleation, albeit at high rates. These two examples illustrate the critical importance to accurately model diffusive bubble growth, in order to accurately calculate the change in bubble nucleation rate, J, throughout the experiment.

[54] During modeling the value of W_{cl} is calculated from equation (7), with σ_∞ based on the work of *Bagdassarov et al.* [2000] and using the maximum value of Δp_s attained during the experiment. The value of the nonclassical nucleation work, W_{nc}, is calculated from equation (14), at the time-dependent value of Δp_s and the value of Δp^* where χ has its minimum. The resultant values of W_{nc}/W_{cl}, as a function of $\xi = \Delta p_s/\Delta p^*$, are shown in Figure 8, which demonstrates that the nucleation work for homogeneous bubble nucleation in rhyolitic melt is significantly lower than would be predicted from CNT. Estimates of W_{nc}/W_{cl} are based on the formulation of *Kashchiev* [2003, 2004] and represent the fractional reduction in nucleation work, resulting from the diffuse

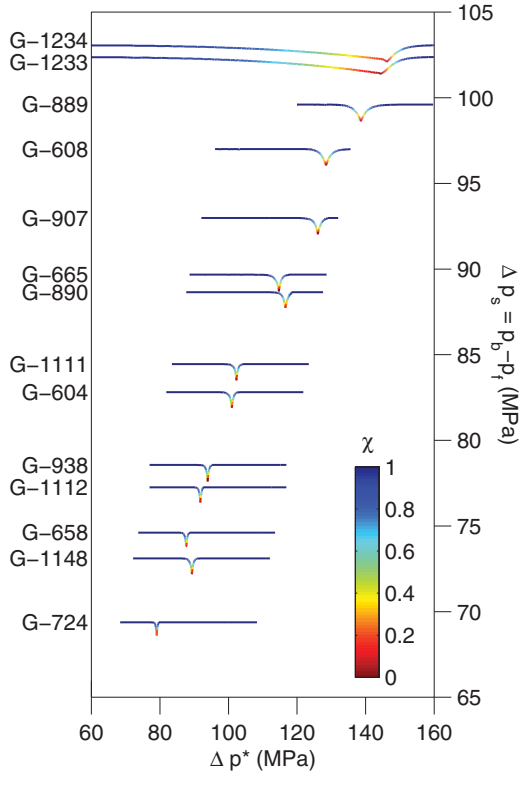

Figure 6. Fit of calculated to observed bubble number density as a function of Δp^*. Each experiment is plotted at its maximum value of Δp_s. For each experiment, the match between observed and calculated values of N_m is quantified as a misfit, $0 \leq \chi \leq 1$, as defined in equations (27a) and (27b). For each experiment, the value of $\chi = 1$ is plotted as a function of Δp^* (abscissa) at the maximum value of Δp_s (ordinate) for the given experiment. Thus, the value of Δp_s is constant for each experiment. The apparent variation in Δp_s for each experiment represents the variation in χ, which is also indicated by the color of the plotted curve, as indicated by the color bar. Only experiments that nucleated bubbles are shown. Note that experiments G-938 and G-1112 have the same value of Δp_s and are shifted slightly upward and downward, respectively, to distinguish them.

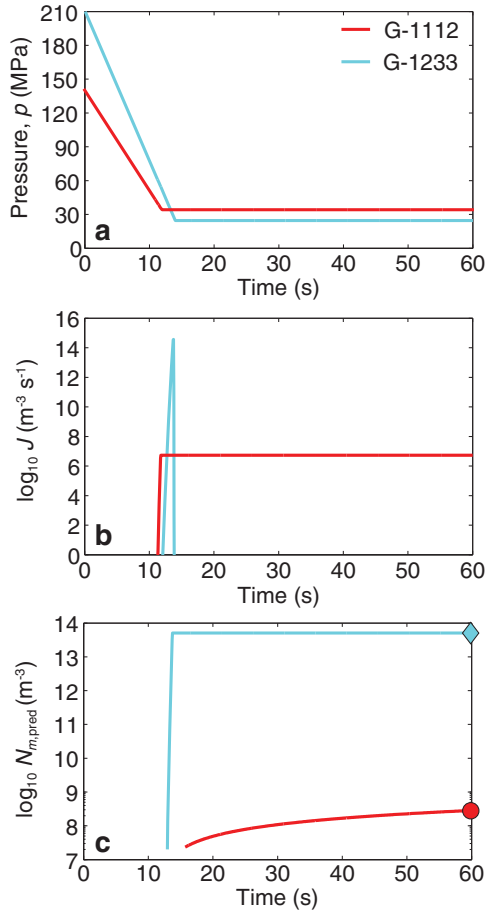

Figure 7. Two illustrative example results from the combined bubble nucleation and growth modeling. Shown are samples G-1112 and G-1233 (see Table 1 for experimental conditions). (a) Modeled pressure, p, as a function of time. (b) Predicted nucleation rate, J, as a function of time. (c) Predicted bubble number density, $N_{m,\mathrm{pred}}$, as a function of time. At the end of the experiment $N_{m,\mathrm{pred}}$ matches the observed value, $N_{m,\mathrm{obs}}$. The lowest value of $N_{m,\mathrm{pred}}$ corresponds to one bubble per volume of sample.

interface between bubble nuclei and surrounding melt phase and ensuing dependence of surface tension on the degree of supersaturation, also observed in other types polymer melts [*Guo et al.*, 2012]. Although it remains to be shown theoretically what precise functional form a nonclassical formulation for nucleation work in silicate melts should have, the approach is in principle valid for one component and multicomponent liquids [*Kashchiev*, 2004].

[55] Figure 9 shows that for all experiments in which bubbles nucleated, the dimensionless nucleation work, $W_{\mathrm{nc}}/k_{\mathrm{B}}T$, depends on Δp_s and falls approximately along the empirical trend

$$W_{\mathrm{nc}}/k_{\mathrm{B}}T = 67.5 - e^{(\Delta p_s/84.5\mathrm{MPa})^6}. \quad (28)$$

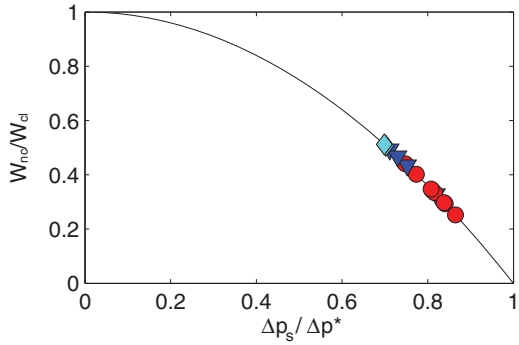

Figure 8. The normalized nucleation work $W_{\mathrm{nc}}/W_{\mathrm{cl}}$, based on the formulation of *Kashchiev* [2003, 2004], given by $W_{\mathrm{nc}}/W_{\mathrm{cl}} = 1-\xi^2$ (equation 14), where $\xi = \Delta p_s/\Delta p^*$ (equation 16). The value of p^* is that, for which the predicted value of N_m, based on the integration of equation (13), is equal to the observed value. Symbols are the same as in Figure 1.

[56] We note that this trend is purely empirical and has no theoretical basis. It is, nevertheless, distinctly different from the trend predicted by classical nucleation theory. For Δp_s approximately <95 MPa the dimensionless nucleation work is almost constant, decreasing only slightly as supersaturation increases. This is a consequence of the dependence of W_{nc} on $\sigma_{\mathrm{nc}}^3/\Delta p_s^2$ (equation 15) and the concurrent increase of σ_{nc} and Δp_s, as shown in Figure 11. The resultant nucleation rates are almost constant, which is shown in Figure 12. In contrast, CNT would predict large increases in nucleation rate (Figure 9) under the same conditions [e.g., *Mangan and Sisson*, 2005]. The trend obtained from our experiments reverses, however, for Δp_s approximately >95 MPa, because σ_{nc} decreases with further increase in Δp_s. This

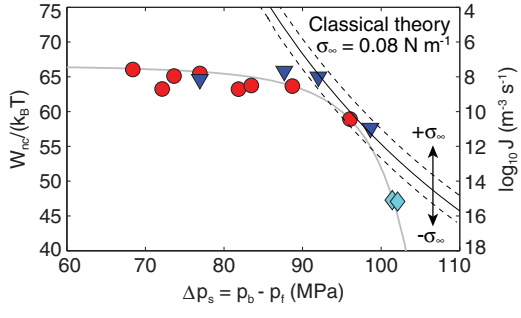

Figure 9. The dimensionless nucleation work, $W_{\mathrm{nc}}/k_{\mathrm{B}}T$, and the nucleation rate, J_{nc}, as a function of Δp_s at which the predicted values of N_m, based on the integration of equation (13), are equal to the observed values. The gray curve represents the empirical fit $W_{\mathrm{nc}}/k_{\mathrm{B}}T = 67.5 - e^{(\Delta p_s/84.5\mathrm{MPa})^6}$. The black curves show the trend predicted by classical nucleation theory at a constant value of σ_∞. Symbols are the same as in Figure 1.

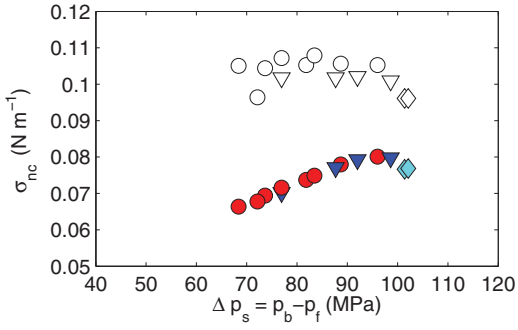

Figure 10. The value of σ_{nc} for the results shown in Figure 8. Symbols are the same as in Figure 1, whereas open black symbols showing the corresponding value of σ_{∞}, based on the work of *Bagdassarov et al*. [2000].

increase in nucleation rate with supersaturation is larger than would be predicted by CNT (Figure 9), presumably because of CNT's assumption of a constant surface tension. One may speculate whether this rapid increase in nucleation rate, compared to CNT, might relax the high decompression rates required by CNT, in order to produce bubble number densities $\gg 10^{14}\mathrm{m}^{-13}$ [*Toramaru*, 2006].

[57] As shown in Figure 10, the empirical fit of equation (28) is able to predict bubble number densities, $N_{m,\mathrm{pred}}$, to within approximately one order of magnitude of the observed value, $N_{m,\mathrm{obs}}$, across six orders of magnitude. We also find that the value of σ_{nc} is always lower than σ_{∞} (Figure 11). This dependence of σ_{nc} and, hence, W_{nc}/k_BT on the degree of supersaturation, Δp_s, is consistent with the work of *Kashchiev* [2003, 2004]. Moreover, the maximum values of W_{nc}/k_BT at which nucleation is observed are similar to those

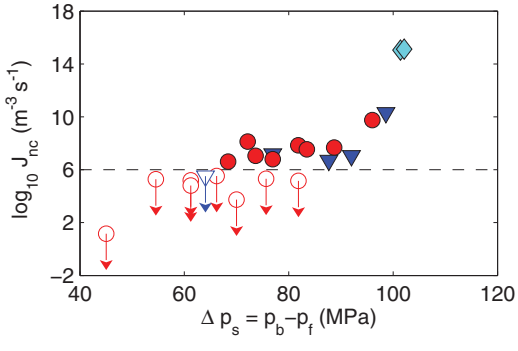

Figure 11. Predicted peak nucleation rates, J_{nc}, for the results shown in Figure 8. The arrows are for experiments during which no bubbles nucleated and indicate that the calculated value of J_{nc} represents an upper bound. The horizontal dashed line is drawn to aid the eye, but corresponds approximately to the inverse product of induction time and sample volume, $1/(\tau_i V)$. Symbols are the same as in Figure 1.

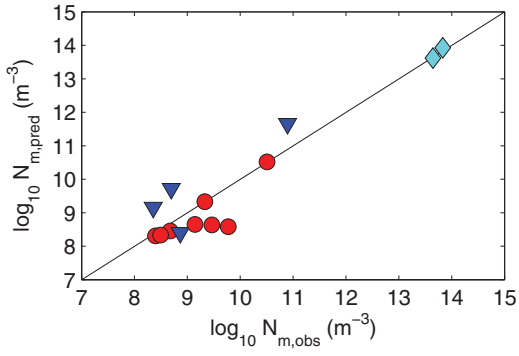

Figure 12. The match between observed and predicted values of N_m, based on the integration of equation (13) for actual values of Δp_s and values of W_{nc}/k_BT that are based on the empirical fit $W_{nc} = 67.5 - e^{(\Delta p_s/84.5\mathrm{MPa})^6}$, shown in Figure 9. Over a range of six orders of magnitude in observed N_m, the misfit between predicted and observed values of N_m is approximately one order of magnitude or less. Symbols are the same as in Figure 1.

obtained from other nucleation experiments [e.g., *Kelton and Greer*, 2010, and references therein].

6. Conclusions

[58] As a result of our integrated study of homogeneous bubble nucleation during decompression experiments of hydrous rhyolitic melt and numerical modeling based on nonclassical nucleation theory, we find that the surface tension between critical bubble nuclei and surrounding melt is smaller than the macroscopically measurable surface tension. This is consistent with a diffuse interface between the nucleating phase and the surrounding metastable liquid, resulting in a dependence of surface tension on the degree of supersaturation. Our results explain the discrepancy between surface tension estimates from bubble nucleation experiments and macroscopic surface tension measurements in silicate melts.

[59] We show that the dependence of nucleus surface tension on supersaturation can in principle be modeled, albeit with the caveat that the difference between the internal pressure of the bubble nucleus and the spinodal is not known a priori, thus introducing an additional parameter. Perhaps the best way forward will be to obtain an empirical formulation for the nucleation work, which is independent of this parameter. For the experiments analyzed herein such an empirical equation predicts homogenous bubble nucleation rates for our experiments to within one order of magnitude of actual values. At low (high) degrees of

supersaturation the nucleation work decreases more gradually (steeply) with increasing supersaturation than predicted by classical nucleation theory. How this departure from the classical theory affects predictions of bubble nucleation during explosive volcanic eruptions requires further work.

Acknowledgments

[60] The authors thank M. Hamada and T. Shea for thoughtful and thorough manuscript reviews. This material is based upon work supported by the National Science Foundation under grant NSF EAR-1019872, NSF IDR-1015069, NSF EAR-0738664, and NSF OCI-0959097. Any opinions, findings, and conclusions or recommendations expressed in this material are those of the author(s) and do not necessarily reflect the views of the National Science Foundation.

References

Adams, N. K., B. F. Houghton, and W. Hildreth (2006), Abrupt transitions during sustained explosive eruptions: Examples from the 1912 eruption of Novarupta, Alaska, *Bull. Volcanol.*, *69*, 189–206, doi:10.1007/s00445-006-0067-4.

Alfano, F., C. Bonadonna, and L. Gurioli (2012), Insights into eruption dynamics from textural analysis: The case of the May, 2008, Chaitén eruption, *Bull. Volcanol.*, *74*, 2095–2108, doi:10.1007/s00445-012-0648-3.

Amon, M., and C. D. Denson (1984), A study of the dynamics of foam growth: Analysis of the growth of closely spaced spherical bubbles, *Polymer Eng. Sci.*, *24*, 1026–1034, doi:10.1002/pen.760241306.

Arefmanesh, A., and S. Advani (1991), Diffusion-induced growth of a gas bubble in a viscoelastic fluid, *Rheol. Acta*, *30*, 274–283, doi:10.1007/BF00366641.

Bagdassarov, N., A. Dorfman, and D. B. Dingwell (2000), Effect of alkalis, phosphorus, and water on the surface tension of haplogranite melt, *Am. Mineral.*, *85*, 33–40.

Blower, J. D., J. P. Keating, H. M. Mader, and J. C. Phillips (2001), Inferring volcanic degassing processes from vesicle size distributions, *Geophys. Res. Lett.*, *28*, 347–350.

Blower, J. D., J. P. Keating, H. M. Mader, and J. C. Phillips (2002), The evolution of bubble size distributions in volcanic eruptions, *J. Volcanol. Geotherm. Res.*, *120*, 1–23.

Cluzel, N., D. Laporte, A. Provost, and I. Kannewischer (2008), Kinetics of heterogeneous bubble nucleation in rhyolitic melts: Implications for the number of density of bubbles in volcanic conduits and for pumice textures, *Contrib. Mineral. Petrol.*, *156*, 745–763, doi:10.1007/s00410-008-0313-1.

Debenedetti, P. G. (1996), *Metastable Liquids: Concepts and Principles*, 411 pp., Princeton Univ. Press, Princeton, N. J.

Gaonac'h, H., J. Stix, and S. Lovejoy (1996a), Scaling effects on vesicle shape, size and heterogeneity of lavas from Mount Etna, *J. Volcanol. Geotherm. Res.*, *74*, 131–153.

Gaonac'h, H., S. Lovejoy, J. Stix, and D. Schertzer (1996b), A scaling growth model for bubbles in basaltic lava flows, *Earth Planet. Sci. Lett.*, *139*, 395–409.

Gaonac'h, H., S. Lovejoy, and D. Schertzer (2005), Scaling vesicle distributions and volcanic eruptions, *Bull. Volcanol.*, *67*, 350–357, doi:10.1007/s00445-004-0376-4.

Gardner, J. E. (2007), Heterogeneous bubble nucleation in highly viscous silicate melts during instantaneous decompression from high pressure, *Chem. Geol.*, *236*, 1–12, doi:10.1016/j.chemgeo.2006.08.006.

Gardner, J. E., and M.-H. Denis (2004), Heterogeneous bubble nucleation on Fe-Ti oxide crystals in high-silica rhyolitic melts, *Geochim. Cosmochim. Acta*, *68*, 3587–3597, doi:10.1016/j.gca.2004.02.021.

Gardner, J. E., and R. A. Ketcham (2011), Bubble nucleation in rhyolite and dacite melts: Temperature dependence of surface tension, *Contrib. Mineral. Petrol.*, *162*, 929–943, doi:10.1007/s00410-011-0632-5.

Gardner, J. E., M. Rutherford, S. Carey, and H. Sigurdsson (1995), Experimental constraints on pre-eruptive water contents and changing magma storage prior to explosive eruptions of Mount St Helens volcano, *Bull. Volcanol.*, *57*, 1–17, doi:10.1007/BF00298703.

Gardner, J. E., R. M. E. Thomas, and C. Jaupart (1996), Fragmentation of magma during Plinian volcanic eruptions, *Bull. Volcanol.*, *58*, 144–162.

Gardner, J. E., M. Hilton, and M. R. Carroll (1999), Experimental constraints on degassing of magma: Isothermal bubble growth during continuous decompression from high pressure, *Earth Planet. Sci. Lett.*, *168*, 201–218.

Giachetti, T., T. H. Druitt, A. Burgisser, L. Arbaret, and C. Galven (2010), Bubble nucleation, growth and coalescence during the 1997 Vulcanian explosions of Soufrière Hills Volcano, Montserrat, *J. Volcanol. Geotherm. Res.*, *193*, 215–231, doi:10.1016/j.jvolgeores.2010.04.001.

Gibbs, J. W. (1961), *The Scientific Papers of J. Willard Gibbs, Ph.D., LL.D. I. Thermodynamics*, pp. 219–331, Dover, New York.

Gonde, C., C. Martel, M. Pichavant, and H. Bureau (2011), In situ bubble vesiculation in silicic magmas, *Am. Mineral.*, *96*, 111–124, doi:10.2138/am.2011.3546.

Gonnermann, H. M., and B. F. Houghton (2012), Magma degassing during the Plinian eruption of Novarupta, Alaska, 1912, *Geochem. Geophys. Geosyst.*, *13*, Q10009, doi:10.1029/2012GC004273.

Gonnermann, H. M., and M. Manga (2007), The fluid mechanics inside a volcano, *Annu. Rev. Fluid Mech.*, *39*, 321–356.

Guo, Z., A. C. Burley, K. W. Koelling, I. Kusaka, L. J. Lee, and D. L. Tomasko (2012), CO_2 bubble nucleation in polystyrene: Experimental and modeling studies, *J. Appl. Polym. Sci.*, *125*, 2170–2186, doi:10.1002/app.36422.

Gurioli, L., B. F. Houghton, K. V. Cashman, and R. Cioni (2005), Complex changes in eruption dynamics during the 79 AD eruption of Vesuvius, *Bull. Volcanol.*, *67*, 144–159, doi:10.1007/s00445-004-0368-4.

Hamada, M., D. Laporte, N. Cluzel, K. T. Koga, and T. Kawamoto (2010), Simulating bubble number density of rhyolitic pumices from Plinian eruptions: Constraints from fast decompression experiments, *Bull. Volcanol.*, *72*, 735–746, doi:10.1007/s00445-010-0353-z.

Hirth, G., G. M. Pound, and G. R. St Pierre (1970), Bubble nucleation, *Metall. Trans.*, *1*, 939–945.

Houghton, B. F., and H. M. Gonnermann (2008), Basaltic explosive volcanism: Constraints from deposits and models, *Chem. Erde*, *68*, 117–140, doi:10.1016/j.chemer.2008.04.002.

Houghton, B. F., R. J. Carey, K. V. Cashman, C. J. N. Wilson, B. J. Hobden, and J. E. Hammer (2010), Diverse patterns of

ascent, degassing, and eruption of rhyolite magma during the 1.8 ka Taupo eruption, New Zealand: Evidence from clast vesicularity, *J. Volcanol. Geotherm. Res.*, *195*, 31–47, doi:10.1016/j.jvolgeores.2010.06.002.

Hui, H. J., and Y. X. Zhang (2007), Toward a general viscosity equation for natural anhydrous and hydrous silicate melts, *Geochim. Cosmochim. Acta*, *71*, 403–416, doi:10.1016/j.gca.2006.09.003.

Hurwitz, S., and O. Navon (1994), Bubble nucleation in rhyolitic melts—Experiments at high-pressure, temperature and water-content, *Earth Planet. Sci. Lett.*, *122*, 267–280, doi:10.1016/0012-821X(94)90001-9.

Kashchiev, D. (2000), *Nucleation: Basic Theory with Applications*, 529 pp., Butterworth-Heinemann, Oxford, U. K.

Kashchiev, D. (2003), Thermodynamically consistent description of the work to form a nucleus of any size, *J. Chem. Phys.*, *118*, 1837–1851, doi:10.1063/1.1531614.

Kashchiev, D. (2004), Multicomponent nucleation: Thermodynamically consistent description of the nucleation work, *J. Chem. Phys.*, *120*, 3749–3758, doi:10.1063/1.1643711.

Kedrinskiy, V. (2009), Hydrodynamic aspects of explosive eruptions of volcanoes: Simulation problems, *Shock Waves*, *18*, 451–464, doi:10.1007/s00193-008-0181-7.

Kelton, K. F., and A. L. Greer (2010), *Nucleation in Condensed Matter: Applications in Materials and Biology, vol. 15, Pergamon Materials Series*, 726 pp., Elsevier, Oxford, U. K.

Kerrick, D. M., and G. K. Jacobs (1981), A modified Redlich-Kwong equation for H_2O, CO_2, and H_2O-CO_2 mixtures at elevated pressures and temperatures, *Am. J. Sci.*, *281*, 735–767.

Klug, C., and K. V. Cashman (1994), Vesiculation of May 18, 1980, Mount St. Helens Magma, *Geology*, *22*, 468–472.

Klug, C., and K. V. Cashman (1996), Permeability development in vesiculating magmas: Implications for fragmentation, *Bull. Volcanol.*, *58*, 87–100.

Klug, C., K. V. Cashman, and C. R. Bacon (2002), Structure and physical characteristics of pumice from the climactic eruption of Mount Mazama (Crater Lake), Oregon, *Bull. Volcanol.*, *64*, 486–501, doi:10.1007/s00445-002-0230-5.

Larsen, J. F. (2008), Heterogeneous bubble nucleatin and disequilibrium H_2O exsolution in Vesuvius K-phonolite melts, *J. Volcanol. Geotherm. Res.*, *175*, 278–288, doi:10.1016/j.jvolgeores.2008.03.015.

Lautze, N. C., and B. F. Houghton (2007), Linking variable explosion style and magma textures during 2002 at Stromboli volcano, Italy, *Bull. Volcanol.*, *69*, 445–460, doi:10.1007/s00445-006-0086-1.

Lensky, N., V. Lyakhovsky, and O. Navon (2001), Radial variations of melt viscosity around growing bubbles and gas overpressure in vesiculating magmas, *Earth Planet. Sci. Lett.*, *186*, 1–6, doi:10.1016/S0012–821X(01)00227-8.

Lensky, N. G., O. Navon, and V. Lyakhovsky (2004), Bubble growth during decompression of magma: Experimental and theoretical investigation, *J. Volcanol. Geotherm. Res.*, *129*, 7–22, doi:10.1016/S0377-0273(03)00229-4.

Liu, Y., Y. X. Zhang, and H. Behrens (2005), Solubility of H_2O in rhyolitic melts at low pressures and a new empirical model for mixed H_2O-CO_2 solubility in rhyolitic melts, *J. Volcanol. Geotherm. Res.*, *143*, 219–235, doi:10.1016/j.jvolgeores.2004.09.019.

Mangan, M. T., and K. V. Cashman (1996), The structure of basaltic scoria and reticulite and inferences for vesiculation, foam formation, and fragmentation in lava fountains, *J. Volcanol. Geotherm. Res.*, *73*, 1–18.

Mangan, M., and T. Sisson (2000), Delayed, disequilibrium degassing in rhyolite magma: Decompression experiments and implications for explosive volcanism, *Earth. Planet. Sci. Lett.*, *183*, 441–455.

Mangan, M., and T. Sisson (2005), Evolution of melt-vapor surface tension in silicic volcanic systems: Experiments with hydrous melts, *J. Geophys. Res.*, *110*, B01202, doi:10.1029/2004JB003215.

Mangan, M. T., K. V. Cashman, and S. Newman (1993), Vesiculation of Basaltic Magma during eruption, *Geology*, *21*, 157–160.

Mourtada-Bonnefoi, C. C., and D. Laporte (1999), Experimental study of homogeneous bubble nucleation in rhyolitic magmas, *Geophys. Res. Lett.*, *26*(23), 3505–3508.

Mourtada-Bonnefoi, C. C., and D. Laporte (2002), Homogeneous bubble nucleation in rhyolitic magmas: An experimental study of the effect of H_2O and CO_2, *J. Geophys. Res.*, *107*(B4), ECV 2–1–ECV 2–19, doi:10.1029/2001JB000290.

Mourtada-Bonnefoi, C. C., and D. Laporte (2004), Kinetics of bubble nucleation in a rhyolitic melt: An experimental study of the effect of ascent rate, *Earth Planet. Sci. Lett.*, *218*(3–4), 521–537, doi:10.1016/S0377-0273(03)00233-6.

Navon, O., and V. Lyakhovsky (1998), Vesiculation processes in silicic magmas, in *The Physics of Explosive Volcanic Eruptions*, edited by J. S. Gilbert and D. W. Sparks, pp. 27–50, Geol. Soc., London., doi:10.1144/GSL.SP.1996.145.01.03.

Navon, O., A. Chekhmir, and V. Lyakhovsky (1998), Bubble growth in highly viscous melts: Theory, experiments, and autoexplosivity of dome lavas, *Earth Planet. Sci. Lett.*, *160*, 763–776.

Ni, H., and Y. Zhang (2008), H_2O diffusion models in rhyolitic melt with new high pressure data, *Chem. Geol.*, *250*, 68–78, doi:10.1016/j.chemgeo.2008.02.011.

Nowak, M., S. B. Cichy, R. E. Botcharnikov, N. Walker, and W. Hurkuck (2011), A new type of high-pressure low-flow metering valve for continuous decompression: First experimental results on degassing of rhyodacitic melts, *Am. Mineral.*, *96*, 1373–1380, doi:10.2138/am.2011.3786.

Piochi, M., M. Polacci, G. De Astis, A. Zanetti, A. Mangiacapra, R. Vannucci, and D. Giordano (2008), Texture and composition of pumices and scoriae from the Campi Flegrei caldera (Italy): Implications on the dynamics of explosive eruptions, *Geochem. Geophys. Geosyst.*, *9*, 1–29, doi:10.1029/2007GC001746.

Polacci, M. (2005), Constraining the dynamics of volcanic eruptions by characterization of pumice textures, *Ann. Geophys.*, *48*, 731–738.

Polacci, M., P. Papale, and M. Rosi (2001), Textural heterogeneities in pumices from the climactic eruption of Mount Pinatubo, 15 June 1991, and implications for magma ascent dynamics, *Bull. Volcanol.*, *63*, 83–97, doi:10.I007/s004450000123.

Polacci, M., L. Pioli, and M. Rosi (2003), The Plinian phase of the Campanian Ignimbrite eruption (Phlegraean Fields, Italy): Evidence from density measurements and textural characterization of pumice, *Bull. Volcanol.*, *65*, 418–432, doi:10.1007/s00445-002-0268-4.

Polacci, M., R. A. Corsaro, and D. Andronico (2006), Coupled textural and compositional characterization of basaltic scoria: Insights into the transition from Strombolian to fire fountain activity at Mount Etna, Italy, *Geology*, *34*, 201–204, doi:10.1130/G22318.1.

Polacci, M., D. R. Baker, L. Mancini, S. Favretto, and R. J. Hill (2009), Vesiculation in magmas from Stromboli and implications for normal Strombolian activity and paroxysmal explosions in basaltic systems, *J. Geophys. Res.*, *114*, B01206, doi:10.1029/2008JB005672.

Proussevitch, A., D. Sahagian, and A. Anderson (1993), Dynamics of diffusive bubble growth in magmas: Isothermal case, *J. Geophys. Res.*, *98*, 22,283–22,307, doi:10.1029/93JB02027.

Sparks, R., and S. Brazier (1982), New evidence for degassing processes during explosive eruptions, *Nature*, *295*, 218–220.

Toramaru, A. (1989), Vesiculation process and bubble-size distributions in ascending magmas with constant velocities, *J. Geophys. Res.*, *94*, 17,523–17,542.

Toramaru, A. (1990), Measurement of bubble size distributions in vesiculated rocks with implications for quantitative estimation of eruption processes, *J. Volcanol. Geotherm. Res.*, *43*, 71–90.

Toramaru, A. (1995), Numerical study of nucleation and growth of bubbles in viscous magmas, *J. Geophys. Res.*, *100*, 1913–1931.

Toramaru, A. (2006), BND (bubble number density) decompression rate meter for explosive volcanic eruptions, *J. Volcanol. Geotherm. Res.*, *154*, 303–316, doi:10.1016/j.jvolgeores.2006.03.027.

Walker, D., and O. Mullins Jr. (1981), Surface tension of natural silicate melts from 1,200–1,500°C and implications for melt structure, *Contrib. Mineral. Petrol*, *76*, 455–462.

Wallace, P. J. (2005), Volatiles in subduction zone magmas: Concentrations and fluxes based on melt inclusion and volcanic gas data, *J. Volcanol. Geotherm. Res.*, *140*, 217–240, doi:10.1016/j.jvolgeores.2004.07.023.

Zhang, Y., R. Belcher, P. D. Ihinger, L. Wang, Z. Xu, and S. Newman (1997), New calibration of infrared measurement of dissolved water in rhyolitic glasses, *Geochim. Cosmochim. Acta*, *61*, 3089–3100.